JGR Solid Earth

RESEARCH ARTICLE
10.1029/2022JB025516

The Hydro-Mechanical Properties of Fracture Intersections: Pressure-Dependant Permeability and Effective Stress Law

Ashley Stanton-Yonge[1], Thomas M. Mitchell[1], and Philip G. Meredith[1]

[1]Rock and Ice Physics Laboratory, Department of Earth Sciences, University College London, London, UK

Key Points:

- The permeability of two intersecting fractures is measured as a function of pressure and compared with independent fracture permeability
- Fracture intersections are shown to be significantly more permeable and less compliant than independent macro-fractures
- We propose a hydro-mechanical model for intersection permeability based on the effective elastic compressibility of the intersection cavity

Correspondence to:

A. Stanton-Yonge,
ashley.sesnic.18@ucl.ac.uk

Citation:

Stanton-Yonge, A., Mitchell, T. M., & Meredith, P. G. (2023). The hydro-mechanical properties of fracture intersections: Pressure-dependant permeability and effective stress law. *Journal of Geophysical Research: Solid Earth*, *128*, e2022JB025516. https://doi.org/10.1029/2022JB025516

Received 30 AUG 2022
Accepted 1 FEB 2023

Author Contributions:

Conceptualization: Ashley Stanton-Yonge, Thomas M. Mitchell, Philip G. Meredith
Formal analysis: Ashley Stanton-Yonge
Funding acquisition: Thomas M. Mitchell, Philip G. Meredith
Investigation: Ashley Stanton-Yonge, Philip G. Meredith
Methodology: Ashley Stanton-Yonge, Thomas M. Mitchell, Philip G. Meredith
Resources: Thomas M. Mitchell, Philip G. Meredith
Software: Ashley Stanton-Yonge
Supervision: Thomas M. Mitchell, Philip G. Meredith
Validation: Ashley Stanton-Yonge
Visualization: Ashley Stanton-Yonge

Abstract Fluid flow through the brittle crust is primarily controlled by the capability of fracture networks to provide pathways for fluid transport. The dominant permeability orientation within fractured rock masses has been consistently correlated with the development of fracture intersections; an observation also made at the meso-regional scale. Despite the importance attributed to fracture intersections in promoting fluid flow, the magnitude of their enhancement of fractured rock permeability has not yet been quantified. Here, we characterize the hydro-mechanical properties of intersections in samples of Seljadalur Basalt by generating two orthogonal, tensile fractures produced by two separate loadings using a Brazilian test apparatus, and measuring their permeability as a function of hydrostatic pressure. We observe that intersecting fractures are significantly more permeable and less compliant than two independent macro-fractures. We formulate a model for fracture intersection permeability as a function of pressure by adding the contributions of two independent fractures plus a tube-like cavity with an effective elastic compressibility determined by its geometry. Permeability measurements during cyclic loading allowed determination of the effective stress coefficient (α in $p_e = p_c - \alpha p_p$) for fracture and intersection permeability. We observe a trend of lower $\alpha_{\text{intersection}}$ values with respect to α_{fracture}, which suggests that the channels controlling fluid flow have a higher aspect ratio (are more tubular) for the intersections relative to independent fractures. Our results suggest that fracture intersections play a critical role in maintaining permeability at depth, which has significant implications for the quantification and upscaling of fracture permeability toward reservoir-scale simulations.

Plain Language Summary Fluids are primarily transported within the shallow crust through networks composed of interconnected fractures. Accurate predictions for the volume and direction of fluid flow through fracture networks are necessary for numerous practical applications. Even though the hydraulic properties of individual fractures and their behavior under increasing depth has been extensively studied, the transport properties of the intersections between fractures have not been quantified. Here, we measure the permeability of two intersecting fractures as a function of increasing pressure and compare it to the permeability of independent fractures. We find that fracture intersections are significantly more permeable than macro-fractures, and are capable of maintaining open pathways under conditions of higher pressure. We propose that the total permeability of an intersection system can be modeled as two independent fractures plus a tube-like cavity that is less sensitive to pressure due to its geometry. These findings suggest that the intersections between fractures might be more relevant for maintaining fluid flow at depth than the fractures themselves, which has significant implications for predicting fluid flow at the fracture network scale.

1. Introduction

The transport of fluids within low porosity rocks is primarily dependant on the capability of fractures to provide channels that can be used as fluid pathways. Fault-fracture meshes form potential channels for large volumes of fluid flow and the hydraulic properties of these networks control the rate and direction of fluid transport through the brittle crust (Caine et al., 1996; Sibson, 1996). Accurate characterization and quantification of the hydraulic properties of fracture networks allows the implementation of realistic fluid flow models, which has numerous practical applications including geothermal exploitation, ore deposit exploration, carbon dioxide storage, and the underground disposal of radioactive nuclear waste.

In fracture-controlled systems, the highest fluid flux occurs where the apertures, densities, and connectivity of fractures are greatest (Cox & Ruming, 2004). Snow (1969) was one of the first to suggest that intersections between fracture and fault planes enhance rock-mass permeability by adding tube-like conduits to the composite structural network. Because both tension and shear fractures form perpendicular to slip vectors and to the

Writing – original draft: Ashley Stanton-Yonge
Writing – review & editing: Ashley Stanton-Yonge, Thomas M. Mitchell, Philip G. Meredith

σ_1/σ_3 plane, their intersection lines commonly lie parallel to the intermediate principal stress axis σ_2 (Cox, 2010; Sibson, 1996) (Figure 1). This observation (among others) has led to the widely accepted model wherein the dominant permeability orientation within anisotropic stress fields is co-axial with σ_2 (Faulkner & Armitage, 2013; Rowland & Sibson, 2004; Sibson, 1996).

At the meso-regional scale, fault intersections have been recognized as highly efficient, long-term and focused fluid conduits for ore deposit formation (Craw, 2000; Piquer et al., 2019; Sibson, 1996), geothermal reservoir location (Rowland & Sibson, 2004), and hydrocarbon leakage (Gartrell et al., 2004). Despite the explicit and implicit relevance attributed to fracture intersections in facilitating fluid flow through the brittle crust and controlling its direction, the transport properties of intersections have received surprisingly little attention to date. Moreover, how high permeabilities are maintained at depth under conditions of increasing confining pressures, where fracture apertures are expected to close, remains a subject of debate.

The issue of fracture closure and fluid flow reduction with increasing effective pressure is of critical relevance for accurate models of fluid flow through the subsurface. Extensive studies have been conducted to characterize the physical properties of individual fractures and their response to stress (Bandis et al., 1983; Brown, 1987; Iwai, 1976; Kranz et al., 1979; Tsang & Witherspoon, 1981; Witherspoon et al., 1980), which have led to a qualitative understanding of the coupled hydro-mechanical behavior of fractures. However, predictive models remain elusive. The search for a direct relationship between stress, normal displacement, and fluid flow through a single fracture has been unsuccessful because stress does not appear to be the link between the hydraulic and mechanical properties of rock fractures. Rather, fracture geometry and compliance appear to hold the key for the interrelationship between contact area and void space, which in turn controls fracture stiffness and fluid flow, respectively (Pyrak-Nolte & Morris, 2000; Tsang & Witherspoon, 1981). As a result, recent efforts to couple the hydro-mechanical properties of rock fractures have been focused on the relationship between fluid flow and fracture stiffness (Petrovitch et al., 2013; Pyrak-Nolte & Nolte, 2016). This relationship, though, is complex and strongly dependant on fracture roughness, which is not commonly accessible.

In addition to externally applied stresses, internal fluid pressure within fractures also has an impact on fluid flow. The concept of effective stress (p_e) is useful to capture in a single quantity all combinations of applied confining pressure (p_c) and pore pressure (p_p) that produce the same effect on a material property of interest, regardless of the individual magnitudes of p_c and p_p (Robin, 1973). If the considered property is fracture permeability, the definition of effective pressure is neither definitive nor universal. Experimental and analytical studies have found that an effective stress law (ESL) for fracture permeability is of the form:

$$p_e = p_c - \alpha p_p, \tag{1}$$

where α is constant for linear elastic materials and, although commonly assumed to be equal to 1, has been shown to range within $0.5 < \alpha \leq 1$ for macro-fractures in crystalline rocks (Bernabe, 1986; Walsh, 1981). The magnitude of α appears to be controlled by the geometry of the passages controlling fluid flow within the fracture, with narrow, crack-like passages displaying an α close to 1, whereas lower values of α ($\approx$0.6) are indicative of passages with more equate, tube-like dimensions (Walsh, 1981). The determination of an ESL for fracture permeability may not only shed light on the geometry of the channels transporting fluids within the fracture, but is also a key aspect to be considered for accurate flow models, particularly within conditions of hydraulic stimulation, such as enhanced geothermal systems (EGS), where pore pressure is cyclically changed through variable fluid injection schemes. Because of the variability in the magnitude of α and its potential significance, we avoid using the term effective pressure when referring to the difference between confining and pore pressure (i.e., $\alpha = 1$), and refer to this quantity as differential pressure throughout this manuscript.

In this study, we aim to characterize and quantify the hydraulic and mechanical properties of fracture intersections. This is achieved by generating synthetic intersections between two orthogonal, tensile fractures produced using a Brazilian test technique in a low-porosity, crystalline rock. Intersection permeability is then measured as a function of differential pressure $p_c - p_p$, and is compared to single fracture and intact rock permeability, measured on the same sample. Permeability was also measured while samples were subjected to a cyclic loading path that allowed us to determine ESLs for both single macro-fractures and fracture intersections. We then propose a model of intersection permeability as a function of differential pressure by assuming that the total permeability of an intersection corresponds to the contributions of the two independent orthogonal fractures plus a tube-like cavity with an elastic compressibility determined by its geometry. This approach allows us to examine the coupled

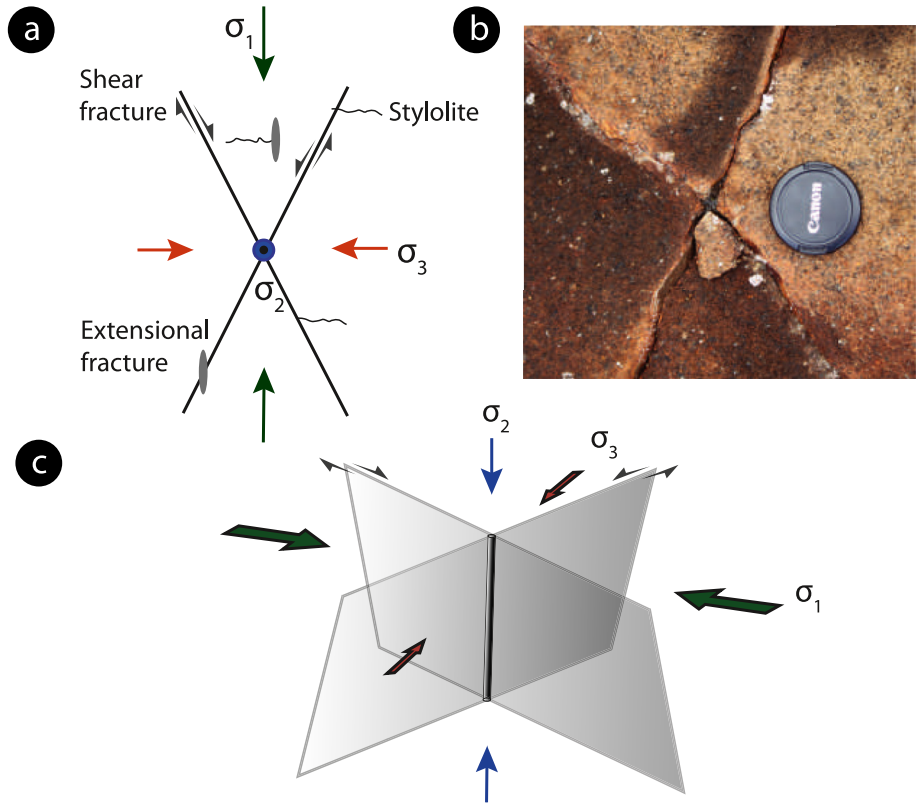

Figure 1. (a) Modified from Sibson (1996) and Cox (2010). Faults, extensional fractures, and stylolites develop within the σ_1/σ_3 plane and their intersections lie co-axial with σ_2. (b) Two intersecting fractures in a hyaloclastite outcrop (Iceland); with the intersection node displaying a higher aperture with respect to the fractures. (c) Conjugate fractures, with their intersection resulting in a tube-like conduit parallel to σ_2.

hydro-mechanical properties of fracture intersections by considering an effective elastic compressibility for the intersection cavity that controls void reduction, and thus fluid flow, with increasing differential pressure. Our results indicate that fracture intersections are significantly more permeable and less compliant than unconnected fractures, which suggests that intersecting nodes can play a critical role in controlling and maintaining fluid flow at depth. These findings have a significant implications for our understanding and modeling of fluid flow through fractured systems at depth, and will help further up-scaling efforts for fluid flow simulations.

2. Materials and Methods

2.1. Sample Material and Preparation

The material selected for this study is Seljadalur Basalt (SB), a columnar-jointed, tholeiitic, basalt from SW Iceland that comprises plagioclase and pyroxene crystals in a glassy matrix. The intact rock has a porosity of 4% as measured by Nara et al. (2011) on the same block of material, and comprises primarily microcrack porosity with sparse microvesicles. Samples were cored from a single block of SB to a diameter of 38.1 (mm) and a length of 40 (mm). Surfaces were then ground flat and parallel to ∓0.002 mm. Cored samples of intact SB were placed in a modified Brazilian test apparatus to produce a tensile axial fracture, resembling Mode I fractures commonly found in nature (Figure 2.1). To accomplish this, the loading rate of the servo-controlled uniaxial load frame was maintained at 0.001 mm/s, equivalent to a diametral strain rate of $2.5 * 10^{-5}s^{-1}$. The loading was stopped immediately after reaching failure.

Where a single, straight, diametral fracture was obtained, the sample was introduced into a hydrostatic permeameter for fracture "seasoning"; the practice of subjecting rock fractures to several pressurization-depressurization cycles (hereinafter referred to as load-unload cycles) to minimize inelastic hysteresis effects (Bernabe, 1987) (Figure 2.2). These samples were subjected to three load-unload cycles in which confining pressure was increased

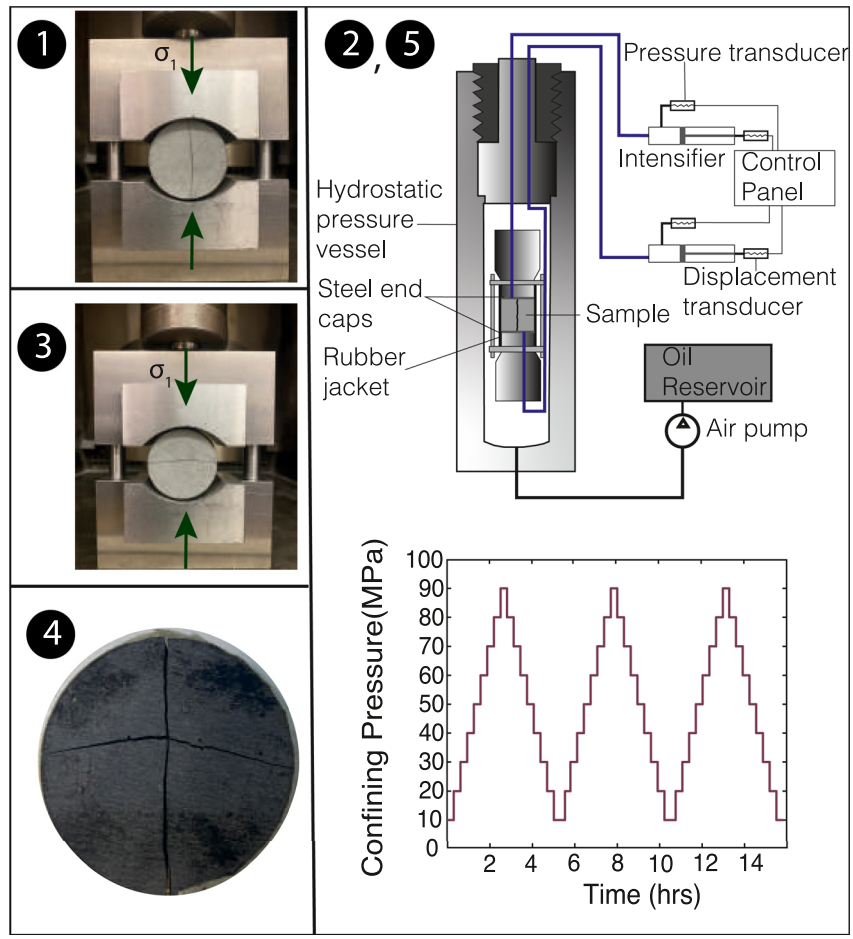

Figure 2. Experimental procedure and equipment to measure the permeability of a single macrofracture and two intersecting fractures on the same sample. (1) A core of intact Seljadalur Basalt is placed in a Brazilian test apparatus to produce a single tensile fracture. (2) The sample is introduced in a servo-controlled, hydrostatic, permeameter where fracture permeability is measured while the sample is subjected to three load-unload cycles of up to 90 MPa confining pressure, in a procedure termed fracture "seasoning." The permeameter diagram was modified from Benson et al. (2005). (3) The sample is then extracted from the permeameter, rotated through 90°, and re-introduced in the Brazilian test apparatus to produce a second, orthogonal macro-fracture. (4) The two orthogonal, diametral fractures produce one axial intersection. (5) The sample with two intersecting fractures is placed again in the permeameter for permeability measurements during another seasoning procedure consisting of three load-unload confining pressure cycles.

in steps of 10 MPa, from 10 to 90 MPa, and then decreased back to 10 MPa in each cycle. Pore pressure was kept constant at 5 MPa during all seasoning cycles and permeability measurements were made at each step during this procedure. The samples were then extracted from the permeameter and re-introduced into the Brazilian test apparatus, rotated through 90° and reloaded in an identical manner to generate a second fracture orthogonal to the first one; thus, producing a single axial intersection from the two diametral fractures (Figure 2.3). Samples with two intersecting fractures were then re-introduced into the permeameter with care taken to ensure that the fractures were fully mated with no shear offset. They were then subjected to the previously described seasoning process, and for subsequent measurements of intersection permeability.

2.2. Permeability Measurements

The permeameter apparatus (Figure 2.2) consists of a steel pressure vessel in which rubber jacketed rock samples can be subjected to hydrostatic confining pressures up to 200 MPa, driven by silicon oil pumped into the vessel by means of a compressed air system (Benson et al., 2005). The sample is placed between two steel end-caps connected to independent single-acting servo-controlled fluid pressure intensifiers capable of raising pore fluid

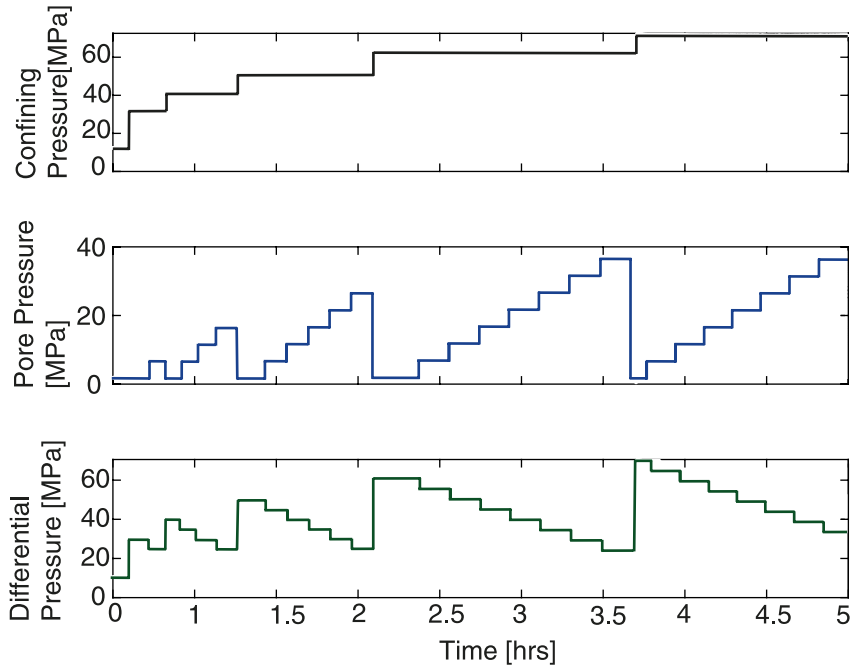

Figure 3. (a) Loading cycle used on samples of Seljadalur Basalt with a single macro-fracture and two intersecting fractures to determine the effective stress law.

pressure up to 70 MPa. Fluid flow is induced by applying a small pressure difference of 0.4 MPa across the sample by keeping the downstream pressure intensifier p_a at a lower pressure than the upstream intensifier p_b. Once steady-state flow Q is achieved across the sample, permeability (k) can be determined directly from Darcy's Law,

$$Q = \frac{-kA_s(p_b - p_a)}{\mu L}, \tag{2}$$

where A_s corresponds to the cross-section area of the sample, L is the sample length and μ is the viscosity of the fluid. To avoid temperature induced permeability fluctuations, the room temperature is maintained constant at 21°C during all the experiments.

2.3. Effective Stress Law Determination

The effective stress parameter (α in Equation 1) is determined following the method described by Walsh (1981) and Bernabe (1986). The procedure is based on the assumption that if an ESL of the form $k(p_c, p_p) = k(p_c - \alpha p_p)$ exists, the family of curves with constant permeability will be graphically represented by parallel straight lines in a p_c versus p_p space, of slope α. To produce these curves, it is necessary to perform a number of permeability measurements at different combinations of p_p and p_c. Fractured samples are first subjected to a fracture seasoning (Figure 2.2), consisting of three load-unload cycles up to a confining pressure of 90 MPa and a constant pore pressure of 5 MPa to ensure reversibility and reproducibility of the permeability evolution, overcoming the irreversible change occurring in the first pressurization stages. Then, the permeability was measured during a fourth loading cycle (Figure 3a) to determine the ESL. In this fourth loading cycle, samples are first subjected to a differential pressure of $p_c - p_p = 30$ MPa, with $p_c = 32$ MPa and $p_p = 2$ MPa. p_c is then increased in 10 MPa steps, while p_p is raised in steps of 5 MPa until reaching the differential pressure of $p_c - p_p = 30$ MPa. This procedure is repeated until confining pressure reaches $p_c = 82$ MPa. During all these steps, a constant difference between the pore pressure intensifiers is held, of $p_b - p_a = 0.4$ MPa.

Permeability results are raised to the power of −1/3 following the procedure of Walsh (1981), and then plotted as a function of confining pressure at fixed values of pore pressure. Linear fitting of these curves allows us to obtain p_p as a function of p_c for constant permeability values. These results are plotted in a p_p versus p_c space, with curves of constant k, the slopes of which represent the effective stress parameter α (see Sections 3.3 and 4.1).

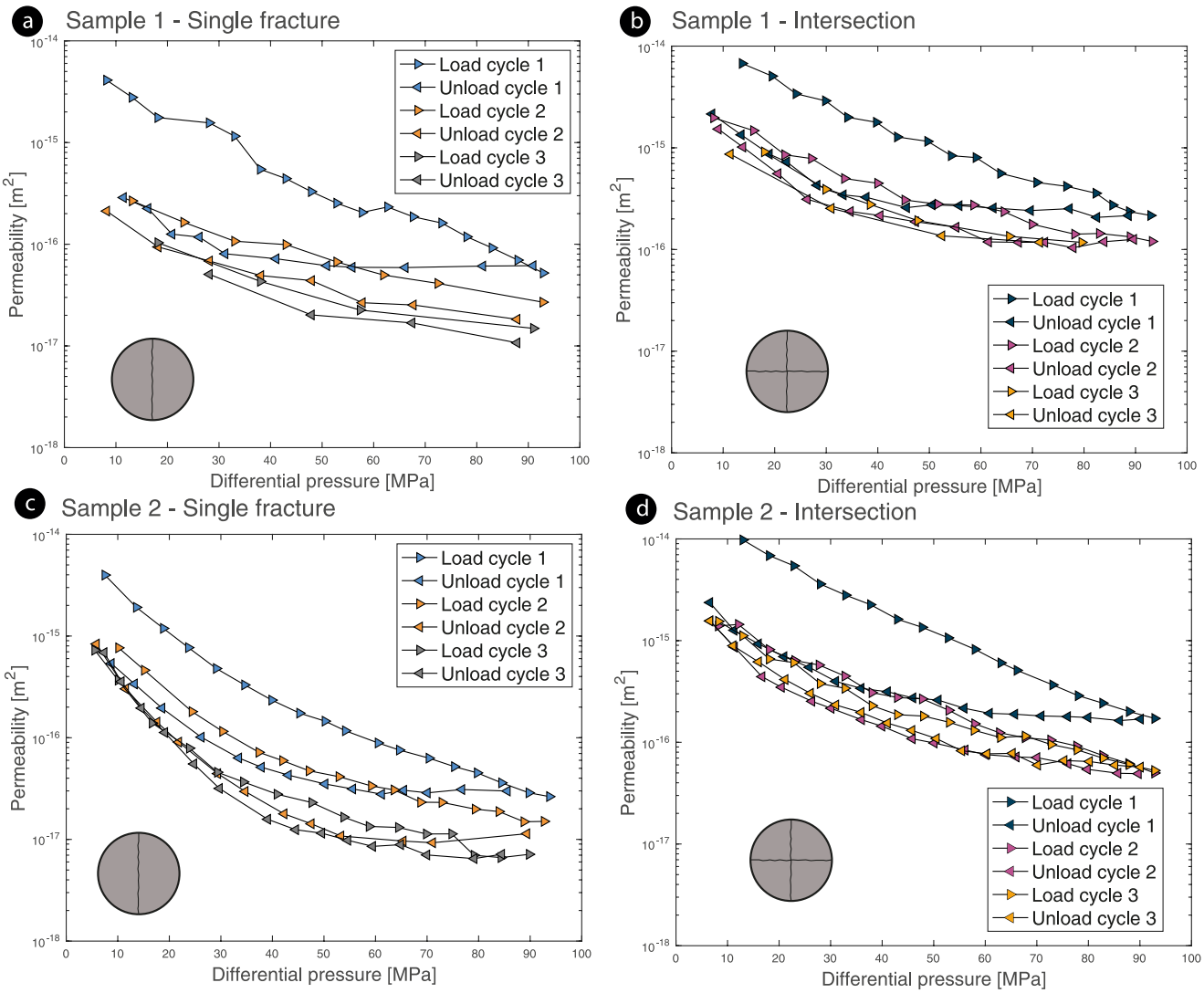

Figure 4. Hysteresis effect detected in permeability measurements during several load-unload cycles of (a) Sample 1 of Seljadalur Basalt (SB) with a single macro fracture, (b) Sample 1 of SB with two intersecting macro-fractures. (c) Sample 2 of SB with a single macro fracture, and (d) Sample 2 of SB with two intersecting macro-fractures.

3. Experimental Results

3.1. Permeability Hysteresis During Load-Unload Cycles

Permeability results during three load-unload cycles with respect to differential pressure for two samples of SB with a single macro-fracture are shown in Figures 4a and 4c and the permeability of the same samples, now containing two intersecting fractures, are shown in Figures 4b and 4d. Results for both samples show that the stress-path dependency, widely known for single fracture permeability (Iwai, 1976; Kluge et al., 2021; Witherspoon et al., 1980), is also detected for intersecting fractures permeability. The permeability measured during the first unloading path is significantly lower than that obtained at equivalent differential pressure during the first loading, with a difference of up to one order of magnitude. Results for the subsequent load-unload cycles consistently indicate that permeability stabilizes during the second loading cycle, with decreasing difference between measurements made during the second and third loading cycles and between their respective loading and unloading paths. In addition, a noticeable difference in slope can be observed between the first and subsequent loading cycles, with the first showing a significantly larger decrease in permeability with increasing differential pressure.

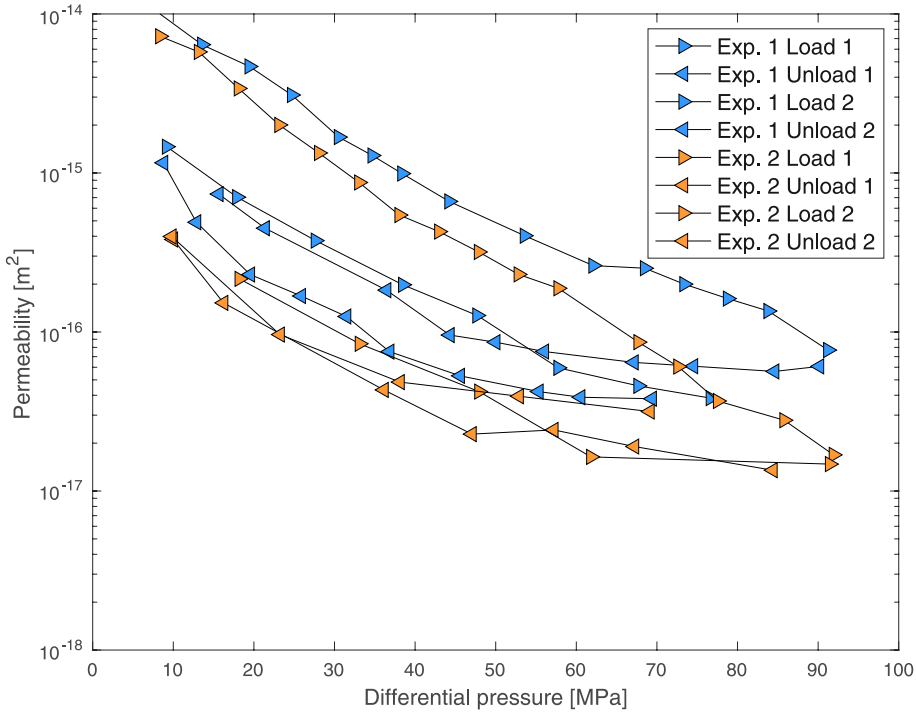

Figure 5. Repeated experiment using the same sample with a single fracture. The sample was first subjected to two cycles of load-unload up to a differential pressure of 90 MPa, after which the sample was removed from the assembly and the halves unmated. The same core was re-introduced in the permeameter for a second set of load-unload cycles.

An additional test was performed in a different sample containing a single macro-fracture to test the reversibility of the loading-path dependency, that is, if the fracture permeability would recover upon complete decompression and fracture unmating. After permeability measurements during two load-unload cycles up to a differential pressure of 90 MPa, a sample with a single macro-fracture was taken out of the permeameter, extracted from the jacket, unmated, re-mated, and re-introduced into the permeameter where it was subjected to two more load-unload cycles. The permeability measured during the repeat experiment is slightly lower than that during the first experiment (Figure 5), though within experimental repeatability. Importantly, however, the hysteresis effect between the first and second loading cycles, that is, the difference in permeability magnitude and sensitivity to pressure between the first and subsequent loading cycles, is maintained and reproduced in the repeat experiment.

3.2. Intersecting Fracture Permeability Compared to Independent Fracture Permeability

The stress-history dependence detected in the previous experiments suggests that the first loading cycle overestimates fracture permeability whereas the unloading and subsequent loading paths represent reversible, elastic, fracture closure. Consequently, we use the results from these loading paths to compare single fracture and intersecting fracture permeability to ensure that elastic deformation processes are the dominant mechanism for fluid flow reduction.

For both samples, we observe a significant increase in permeability when a second, intersecting fracture is introduced in a sample containing a single fracture. This difference is larger at higher differential pressure (Figure 6). In addition, the dependency of permeability on differential pressure measured during unloading, after two pressurization cycles to minimize irreversible effects, also changes and becomes less marked. Both samples exhibit similar behavior in terms of the relative difference between single fracture and intersecting fractures permeability, and in the reduced sensitivity to pressure displayed by samples containing two intersecting fractures.

3.3. Effective Stress Law for Single Fracture and Intersecting Fracture Permeability

The cross-plot method of Walsh (1981) was used to estimate the effective stress coefficient (ESC) for single fracture and intersecting fracture permeability. Constant permeability curves are plotted in a p_c versus p_p space

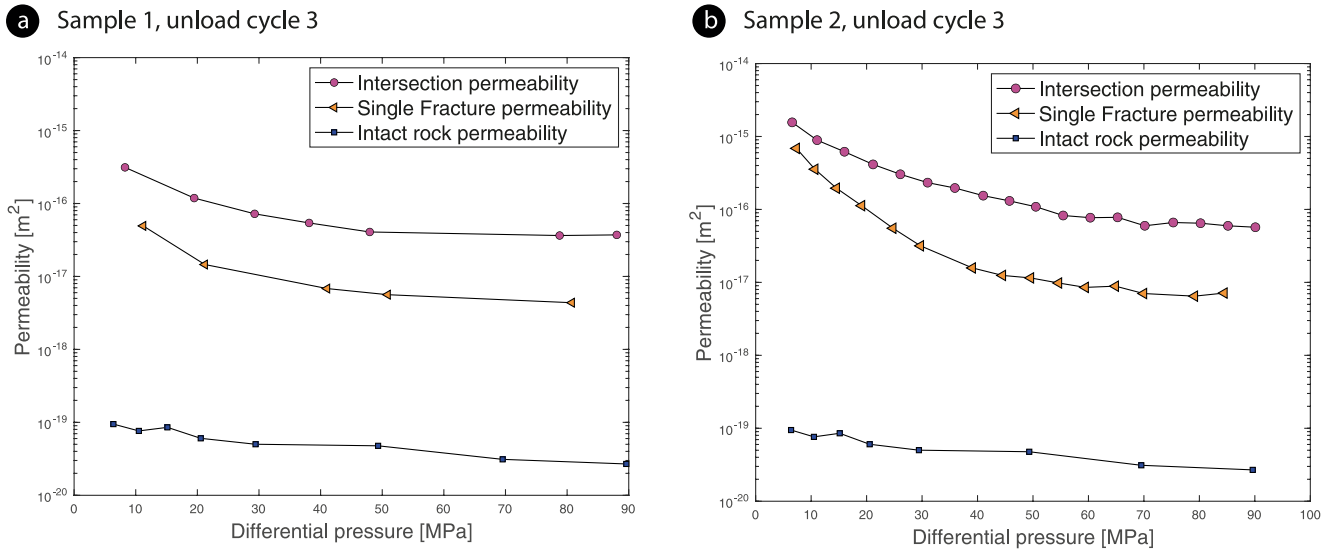

Figure 6. Permeability with respect to differential pressure for a single macro-fracture and two intersecting fractures during the third unload cycle, (a) Sample 1 and (b) Sample 2.

(Figure 7) whose slope represent the ESC α. For a single macro-fracture, α ranges from 0.84 to 1, with an average of 0.91, whereas for intersecting fractures α ranges from 0.77 to 0.86 with an average of 0.81, indicating a consistent tendency of lower ESC values for the intersecting fractures compared with a single fracture.

4. A Physical Model for Intersecting Fractures Permeability

4.1. Fracture and Intersection Permeability as a Function of Stress

In this section we attempt to produce a model for intersection permeability as a function of differential pressure $p_c - p_p$. We approach the problem of fluid flow through intersecting fractures as the superposition of fluid flow through two independent fractures plus a cavity representing the intersection between them. To achieve this, we first need to fit the single fracture permeability data to a predictive model of flow through a single fracture as a function of stress.

The link between the hydraulic and mechanical behavior of rock fractures (i.e., the relationship between permeability and stress) is complex and indirect because fluid flow is controlled by the size and spatial distribution of

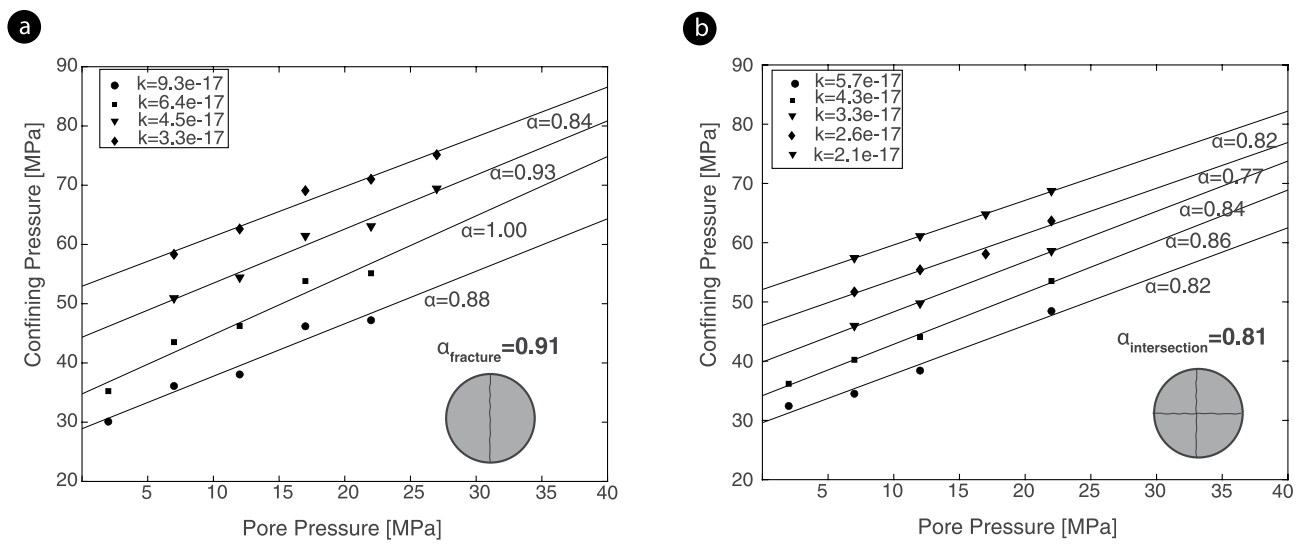

Figure 7. Effective stress coefficient (α) determination for (a) Seljadalur Basalt (SB) with a single fracture and (b) SB with two intersecting fractures.

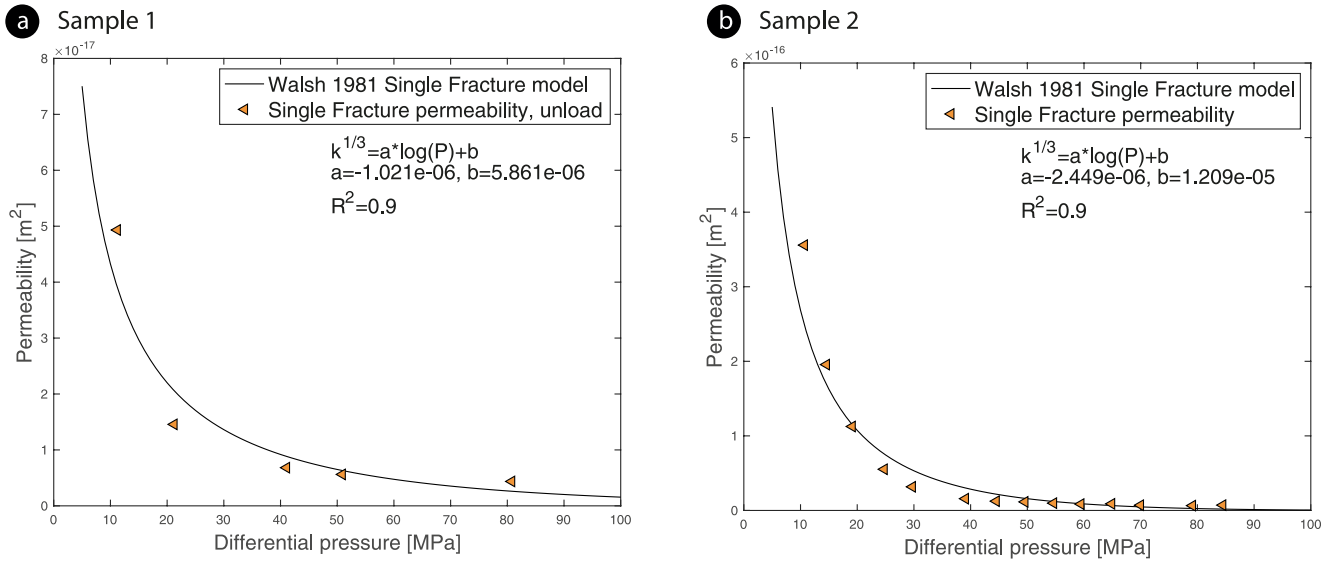

Figure 8. Single fracture permeability data fit to Walsh (1981) model with a coefficient of determination for (a) Sample 1 and (b) Sample 2.

void spaces whereas the mechanical deformation of a fracture is defined by the strength and number of asperities (Jaeger et al., 2009; Pyrak-Nolte & Nolte, 2016). Significant efforts have been made to establish the nature of the coupled hydro-mechanical properties of fractures in rock, for which several physical and empirical models have been proposed. These models include a "bed of nails" approach for fracture asperities (Gangi, 1978), a void aperture model that takes into account fracture roughness (Tsang & Witherspoon, 1981), an effective conductance model derived from heat conduction theory (Walsh, 1981) and an elastic contact model between rough surfaces whose topography is determined by a probability density function (Brown, 1987; Brown & Scholz, 1985). Of these models the most well-known and widely used is that of Walsh (1981), which has the major advantage of considering fractures under effective pressure as opposed to normal stress. Although its analytical expression is difficult to evaluate, it can be simplified to an expression of the form:

$$k_f^{1/3} = A - B\log(p_c - p_p), \tag{3}$$

where k_f is the permeability of a single fracture and A, B are empirical constants that depend on the distribution of asperities and thus are related to the roughness of the fracture surfaces. Several empirical studies have fitted fracture permeability data to expressions of the same form (Bandis et al., 1983; Jones, 1975; Zhao & Brown, 1992), supporting the applicability of the model. Our experimental data from single fracture permeability measurements after three load-unload cycles for both samples 1 and 2 were fitted to Equation 3, with a coefficient of determination $R^2 = 0.9$ (Figure 8). Following this, the permeability of the total system comprising two independent orthogonal fractures and an intersection cavity (k_{tot}) is modeled as,

$$k_{tot} = 2k_f + k_{int}, \tag{4}$$

where k_{int} is the permeability of the intersection cavity. By measuring k_{tot} directly, and assuming that k_f is known from its fit to Equation 3, we can use subtraction to obtain k_{int} from Equation 4 and calculate the initial permeability conducted through the intersection cavity k_{i0} at an initial pressure p_0 (Figure 9).

The flux q conducted through the intersection cavity at p_0 can be determined by substituting k_{i0} in Equation 2. By considering the initial assumption of the cavity having a circular shape, we can calculate the initial equivalent radius of the cavity r_{i0} using the Hagen-Poiseuille equation:

$$q = \frac{\pi r_{i0}^4}{8\mu L}. \tag{5}$$

This results in an equivalent "pipe" with an effective initial radius of $r_{i0} = 19.9$ μm for sample 1 and $r_{i0} = 25$ μm for sample 2. We can now calculate the radial displacement δu_r of these initial circular pipes with increasing

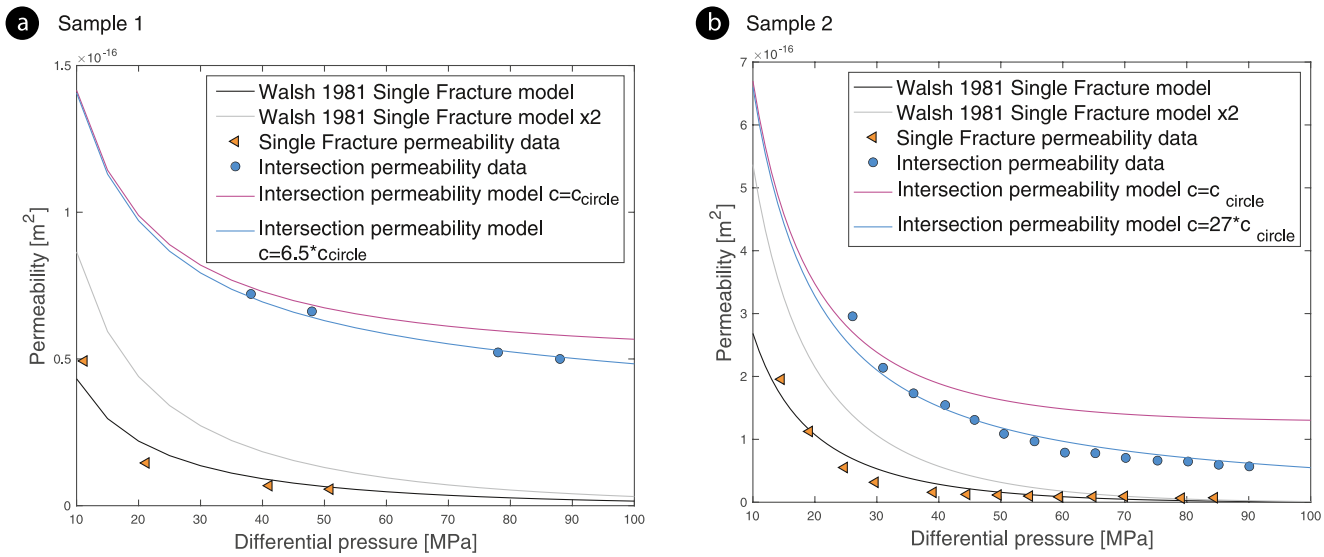

Figure 9. (a) Total permeability model ($2k_f + k_{int}$) as a function of differential pressure considering an elastic compressibility for the intersection cavity (c) equal to that of a circular cross-section (red curve) and a compressibility 6.5 times larger than that of a circular cross section (blue curve). The predicted permeability of two unconnected fractures ($2k_f$) is shown in gray while single fracture permeability (k_f) is shown in black. Single fracture and intersecting fractures permeability data points are shown in orange triangles and blue circles, respectively. An increased effective compressibility is necessary to explain the pressure-dependency of the intersection cavity. (b) Analysis from (a) applied to sample 2 gives an effective compressibility for the intersection 27 times that of a circular cavity.

differential pressure using the plane strain elastic solution of a circular hole subjected to isotropic, differential pressure ($p_c - p_p$) (Pollard, 1973):

$$\delta u_r = \frac{(p_c - p_p) r_{i0}}{E}(4 - 4\nu)(1 + \nu), \tag{6}$$

where E, ν are the Young modulus and Poisson's ratio, respectively. However, we find that the change in radius, and therefore flow rate, with increasing pressure is not sufficient to explain the pressure-dependency of the derived k_{int}. This suggests that the experimental intersection flow paths are more compressible than an equivalent cavity of circular cross-section. Therefore, we multiply δu_r by a factor c that is the ratio of the compressibility of the intersection, normalized to the compressibility of a circular cavity, and find that intersection permeability data can be fitted by considering that the cavity has an "effective" compressibility 6.5 times higher than that of an equivalent circular hole for sample 1 and a compressibility of $c = 27c_{\text{circle}}$ for sample 2. Combining Equations 2, 5, and 6, an expression for the permeability of an intersection cavity as a function of differential stress thus becomes:

$$k_{int} = \frac{\pi r_{i0}^4}{8A_s}\left(1 - \frac{c}{E}(p_c - p_p)(4 - 4\nu)(1 + \nu)\right)^4. \tag{7}$$

4.2. Compressibility Estimation From Cavity Geometry

The elastic compressibility of a cavity in 2D can be defined as the relative change in area produced per unit change in hydrostatic loading. Zimmerman (1986) and Tsukrov and Novak (2002) explored different approaches to determine the compressibility of cavities with irregular geometries, including analytical expressions through the complex variable method and numerical conformal mapping. They found that a simple, reasonably accurate estimation of compressibility for irregular geometries normalized to the compressibility of a circular cavity, can be calculated within an error of 5%–7% with respect to analytical solutions as:

$$c = \frac{c_{\text{cavity}}}{c_{\text{circle}}} = \frac{P^2}{4\pi A_c}, \tag{8}$$

where P and A_c correspond to the cavity perimeter and area, respectively. Sample 1 was saw-cut in two separate locations and polished to make thin sections. The resulting intersection cavity perimeter was traced from optical

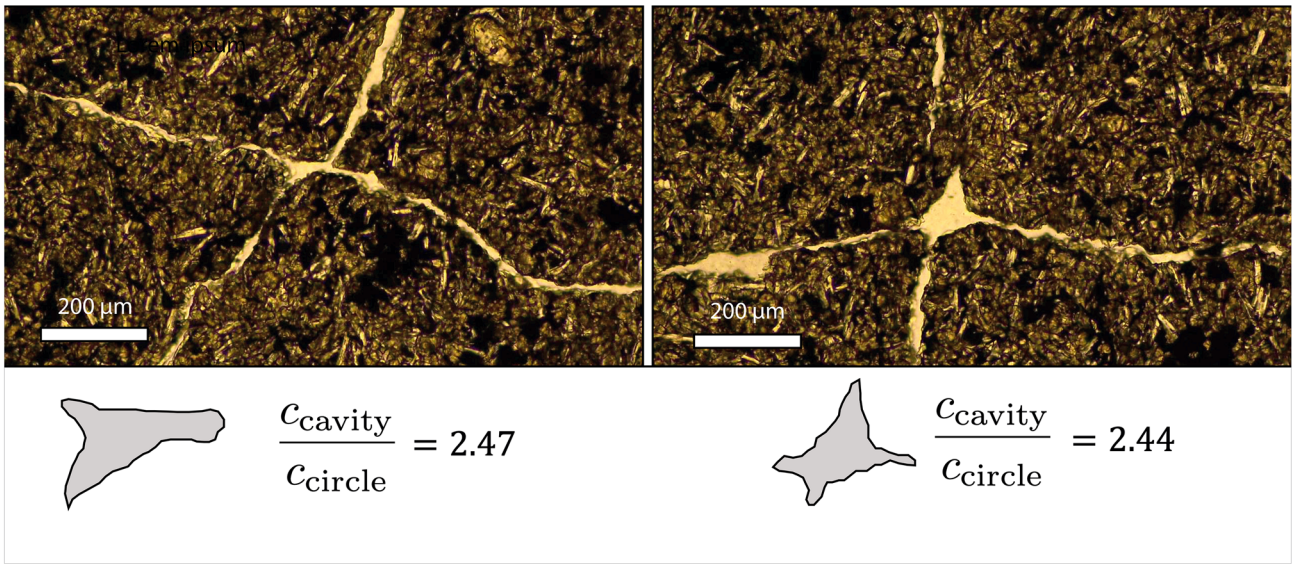

Figure 10. Two thin sections from sample 1. The intersection cavities were traced and the compressibility of the resulting geometries (c_{cavity}) normalized by the compressibility of an equivalent cavity of circular geometry (c_{circle}) were estimated using Equation 8.

microscope images (Figure 10), which allows us to estimate P and A_c, and calculate a normalized compressibility of $c = 2.46$ (Figure 10).

This estimate for the normalized compressibility of the intersection cavity is somewhat lower than the value of $c = 6.5$ for the effective compressibility determined by fitting the area reduction from the intersection permeability model. This differences is to be expected for several reasons. First, the flow rate along the flow path provided by the intersection cavity is controlled by its smallest aperture (cross-sectional area). As can be seen in Figure 10, the geometry of the intersection cavity is highly irregular, and the two measured sections are unlikely to represent the section of minimum aperture along the intersection path length. Second, the estimate of P and A_c from the thin section images is necessarily limited by the scale of the image pixel size. Hence, we need to consider the complexity in determining the "true" perimeter of a rough cavity; equivalent to the emblematic issue of calculating the length of a rocky coastline (Mandelbrot, 1982). The perimeter of such an irregular feature is a problem in fractal geometry, and depends on the measuring scale; as the measurement scale decreases, the measured perimeter increases without bound (i.e., the geometry is non-rectifiable).

By assuming that the cavity boundary is self-affine, a feature that has been widely attributed to the roughness of rock fracture surfaces (Lee et al., 1990), we can calculate its fractal dimension (D) from

$$D = \frac{\log N}{\log \frac{1}{r}}, \tag{9}$$

where N is the number of scale measures of length r that sum to the perimeter length. We obtain that $D = 1.51$ for our cavity boundary. Using this relationship, we find that the fitted effective compressibility of $c = 6.5$ can be obtained by simply considering a measuring scale that is only modestly smaller (x0.73) than that of the resolution of the optical images. In consequence, the intersection compressibility estimation obtained from the fitting of the experimental data is in good agreement with that obtained from the geometry of the cavities. The variability in geometry of intersection cavities noted above is reinforced by our estimate of the effective compressibility of the intersection cavity from sample 2. This gives a value of $c = 27$, four times higher than for sample 1. Whilst this difference may seem significant, the important point is that both estimates indicate that high aspect ratio intersection cavities are considerably less compressible than low aspect ratio cracks, whose compressibility, normalized to that of a circular cavity, is of the order of 1,000 for cracks with an initial aspect ratio of 0.001 (Walsh, 1965).

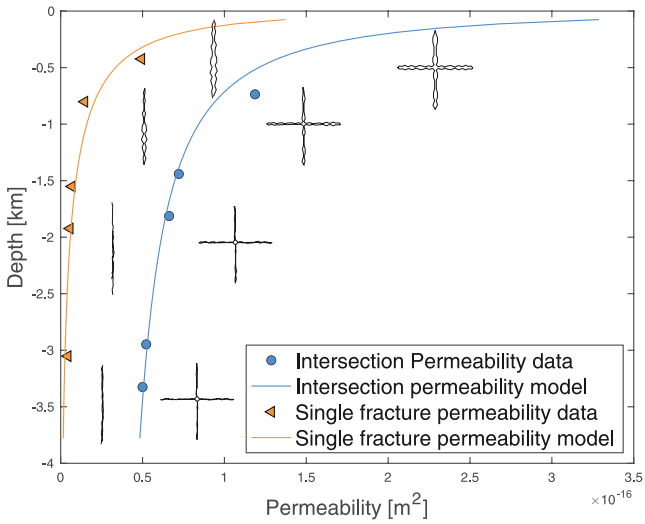

Figure 11. Single fracture and intersecting fracture permeability as a function of depth, considering a rock density of 2700 $\frac{kg}{m^3}$. Both the experimental data and the fitted models are plotted. For the single fracture, the model corresponds to the empirically fitted expression of Walsh (1981), while for the intersecting fractures it corresponds to the superposition of two fractures plus a cavity whose permeability as a function of stress is determined by Equation 7. Schematic representations of crack and intersecting fractures closure with increasing depth are also shown.

5. Discussion

5.1. Intersections Role in Maintaining Fluid Flow at Depth

The experimental results of intersecting fracture permeability with respect to single fracture permeability, measured on the same sample, indicate that intersections are not only significantly more permeable than individual macro-fractures but are also capable of maintaining this higher permeability under conditions of increasing confining pressure, which we propose is a result of the intersection cavity being less compliant than the macro-cracks. This finding has significant implications for the understanding, quantification, and predictability of fluid flow through fractured systems in the subsurface. Permeability (measured and modeled) for a single fracture and intersecting fractures are plotted as a function of depth by considering a rock density of 2700 $\frac{kg}{m^3}$ in Figure 11. It can be observed that both macro-fracture and intersection permeability display a rapid decline within the first kilometer depth in the crust, after which both approach asymptotically to a residual permeability value at greater depth. However, it is interesting to note that, according to the single fracture permeability model that we consider here, adding more but unconnected macro-fractures significantly increases the permeability of the fractured system at low confining pressures, but this increase decreases rapidly at higher confining pressure. This occurs because low aspect ratio macro-fractures close easily with increasing confining pressure, and the permeability decreases with the cube of the crack aperture. This observation is supported by experimental data by Nara et al. (2011), who also measured permeability of fractured samples of SB and observed that the permeability of samples with three unconnected macro-fractures was significantly higher than for samples with a single macro-fracture at low confining pressure, but that the relative difference became much smaller at pressures above about 40 MPa (equivalent to 1.5 km depth) (Figure 12). By contrast, intersection permeability maintains its higher magnitude even at elevated effective confining pressure.

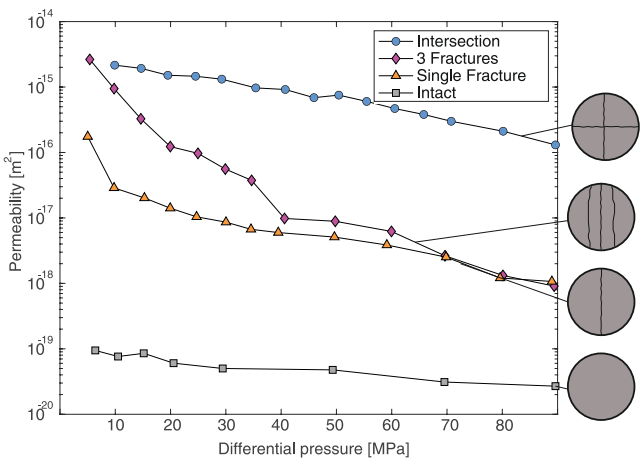

Figure 12. Permeability of Seljadalur Basalt with two intersecting fractures, three unconnected macro-fractures, a single macro-fracture and an intact sample, all measured in different samples. Three unconnected macro-fractures initially display high permeability, comparable to intersection permeability, but rapidly decreases with differential pressure until approaching the same permeability as a single fracture. Measurements of single fracture and three unconnected fractures permeability are from Nara et al. (2011).

5.2. Implications of Intersection Permeability for Up-Scaling and Fracture Network Fluid Flow Modeling

The hydraulic properties of single fractures are the basic building block of realistic fluid flow models through fractured systems, as they are the key input for fluid flow simulations through fracture networks in the subsurface. One approach to upscale the properties of individual fractures to reservoir-scale fractured systems is by means of Discrete Fracture Network (DFN) modeling, in which the geometrical properties of a fracture network (i.e., orientation, length, aperture, spacing) are assessed statistically from analog outcrop analyses and/or borehole datasets so that a prediction of the fracture network configuration at a certain depth can be made (Cacas et al., 1990). Fluid flow through the network is then solved numerically to predict the volume, rate, and direction of fluid flow through the system of composite fractures, usually modeled as elliptical disks, each with a prescribed hydraulic conductivity, usually derived from statistically inferred fracture apertures and the cubic law (de Dreuzy et al., 2001, 2002; Xu & Dowd, 2010).

Our findings suggest that, below a certain depth, the channels for fluid flow provided by the intersection between fractures might be significantly more relevant than the fractures themselves. An implication of this result is that fluid flow through fractured systems could be simplified to the intersection lines of the network and their connectivity. This approach is not new, for example, Cacas et al. (1990) proposed a DFN model in which flow occurs through "bonds" joining fractures, which was based on observations by

Gentier (1986) and Tsang and Tsang (1987) that flow within a fracture is linear rather than two dimensional and can be considered as a series of one-dimensional "flow tubes." To implement such an approach based on our experimental data would imply the need to replace the hydraulic properties of fractures by those of intersections as basic input parameters. Moreover, if the full composite fractured system is considered, our results indicate that different input parameters should be ascribed to the intersecting nodes and lines for realistic results. In short, to consider our findings of intersection permeability and expand the knowledge on the hydraulic properties of intersections, for example, in different lithologies, appears to have significant relevance and practical applications for up-scaling efforts and fluid flow simulations.

5.3. Effective Stress Law for Fractures and Intersections: Fluid Pathways Geometries and Implications for Hydraulic Stimulation

An ESL defines the combinations of confining pressure and pore pressure which produce the same effect on a material property of interest, regardless of the magnitudes of p_c and p_p. The form of the effective stress expression depends on the property considered. In this study, the property of interest is fracture permeability, which is controlled by the configuration of the passages that transport fluids and their response to stress. Because we are dealing with isotropic stresses, flow rate can be considered equal for stress states that produce the same volume of fluid pathways. This assumption allows us to consider fracture permeability ESL equal to that of elastic pore volume variation, for which analytical expressions have been previously derived (Robin, 1973; Walsh, 1981). This results in an ESL of the form shown in Equation 1.

Walsh (1981) evaluated Equation 1 for a circular cross-section channel/pore and found that $\alpha = \frac{2(1+\nu)}{5-2\nu}$, where ν is the Poisson's ratio of the bulk rock. For $\nu = 0.25$, α becomes 0.56 whereas evaluating Equation 1 for elliptical channels shows that α increasingly approaches 1 for lower aspect ratio elliptical cross-sections (i.e., for more elongated ellipsoidal geometries), and the ESL thus approaches Terzaghi's effective pressure law where $\alpha = 1$ (Bernabe, 1986). This analytical result is consistent with experimental data by Kranz et al. (1979), which supports the conclusion that the ESL for fracture permeability depends on how the volume of the flow passages varies with changes in confining and pore pressure, and ranges between 0.56 and 1. The magnitude of α within this range depends on the aspect ratio of the channels controlling fluid flow, with narrow, crack like pathways having ESL coefficients closer to 1, and channels with more equate dimensions having a lower coefficient.

According to this conclusion, one would expect that the ESC for fluid flow through macro-fractures should differ from that of intersecting fractures due to the presence of the intersection cavity, which displays a higher aspect ratio relative to the narrow cracks. The results for effective stress coefficients determination using the cross-plot method shown in Figure 7 indicate that α_{fracture} ranges from 0.84 to 1, with an average of 0.91, whereas $\alpha_{\text{intersection}}$ ranges from 0.77 to 0.86 with an average of 0.81. The trend of lower magnitudes for $\alpha_{\text{intersection}}$ relative to α_{fracture} supports the hypothesis that fluid flow through the intersection between fractures is controlled by a channel with relatively higher aspect ratio compared to the pathways provided by lower aspect ratio fractures.

Bernabe (1986) found a significant stress-path dependency for the ESC for permeability of fractured granite, with a variability in α magnitudes of up to 0.4. In the present study, we subjected our samples to "seasoning" to overcome the inelastic processes that obscure the elastic behavior of fracture permeability before applying the cyclic loading path for ESL determination. The low variability seen in our ESL coefficient results suggests that the stress-path dependency was overcome when ensuring fully elastic deformation mechanisms after several load-unload cycles. However, ESL coefficient calculations should be made during unloading to confirm this.

To determine an expression for the ESL of fractured rock permeability, or rather, to establish whether it diverges from Terzaghi's ESL $p_e = p_c - p_p$, is relevant for a number of practical applications, namely any circumstance in which pore pressure is cyclically changed through fluid injection into reservoirs (e.g., geothermal, hydrocarbon). For example, EGS rely on hydraulic stimulation of fractured reservoirs (among other types of stimulation) to maintain the productivity and permeability of wells. An ESL of the form $p_e = p_c - \alpha p_p$, with $\alpha < 1$ effectively means that pore pressure has a lesser effect on fracture permeability than that of confining stress. This is contrary to the implications of an ESL with $\alpha = 1$, where pore pressure and confining pressure have equal, opposing, effects on permeability. In practical terms, an α of 0.8 will result in an injection scheme designed with Terzaghi's ESL being 20% less efficient in maintaining permeability than expected. In particular, because in this work we are proposing that the more tubular pathways provided by intersections are able to continue controlling fractured

reservoir permeability below 1.5 km depth, it might be more realistic to consider conservative magnitudes of α when designing injection schemes for deep reservoirs.

5.4. Mechanisms Responsible for the Fracture Permeability Hysteresis Effect

The stress-path dependency of fracture permeability detected during cyclic pressurization and depressurization measurements has been widely observed previously (Bandis et al., 1983; Iwai, 1976; Kluge et al., 2021; Witherspoon et al., 1980). Here, we show that the same stress path dependency behavior can be expected for samples with two intersecting fractures. Single fracture and fracture intersection permeability are consistently higher and more sensitive to pressure during the first pressurization cycle. During depressurization, permeability does not recover to its initial magnitude, and several load-unload cycles are needed for fracture permeability curves to become fully elastic and reproducible.

This stress-path dependency has been associated with inelastic deformation mechanisms due to which a portion of the pores and cracks do not fully re-open during unloading thus causing a reduction in permeability between the first and subsequent loading cycles. These inelastic processes have been attributed to: (a) regions of oblique contact between the fracture surfaces were shear stresses develop locally, causing frictional sliding at the micro scale (Scholz & Hickman, 1983), (b) plastic (Yoshioka, 1994) and/or brittle (Milsch et al., 2016) deformation of asperities coming into contact, leading to a permanent increase in contact area, (c) clogging of the fluid flow channels by fine-grained material produced from crushed asperities (Vogler et al., 2016) and (d) time-dependant fracture closure (Milsch et al., 2016). The question of which of these corresponds to the dominant process responsible for fracture permeability hysteresis remains enigmatic.

Measurements of fracture surface topography before and after cyclic hydrostatic pressurization (Brown & Scholz, 1986; Hofmann et al., 2016; Kluge et al., 2021) and simulations of rough surfaces coming into contact under normal stress (Yoshioka, 1994) have revealed that permanent deformation across the fracture surfaces manifests as a reduction in height of the summits of the surface asperities. This permanent damage does not affect height distribution, and therefore the self-affinity and fracture roughness exponent above grain scale, but it does alter the aperture distribution, causing a permanent aperture reduction. This observation indicates that some of the hysteresis in fracture permeability is caused by permanent deformation of asperities. This is also concluded by Milsch et al. (2016), who suggested that fracture contact area adjusts to counterbalance the highest applied stress and the unconfined compressive strength of the material. A process of this sort may be the one responsible for the stress memory effect observed by Kluge et al. (2021), in which fracture surfaces record the highest prior applied stress, which manifests as a transition in fracture stiffness, from linear to non-linear, when the previous highest applied stress is exceeded.

We were interested in exploring the reversibility of the processes causing the hysteresis effect in fracture permeability, for which we performed a repeated pressurization experiment after the sample was extracted from the permeameter, unmated, re-mated, and re-introduced into the permeameter (Figure 5). Results show only a slight variation between the original and repeated fracture permeability measurements. However, it is interesting to note that the hysteresis effect in which the depressurization and subsequent pressurization-depressurization paths are less permeable and pressure sensitive than the initial pressurization path was reproduced in the second set of experiments. The repeatability of the hysteresis effect may be an indication that micro frictional sliding is the dominant process causing the stress-path dependency in fracture permeability between the first and subsequent pressurization cycles, and that this process is reversible.

The fact that samples with intersecting fractures also display stress-path dependency is attributed to the influence of the macro-fractures in the total permeability of the system; the intersection cavity should not be significantly influenced by the mentioned inelastic deformation processes under the hydrostatic pressure conditions considered in this study. However, the same cannot be said when anisotropic stress fields are applied. Increasing deviatoric stresses would lead to slip across one of the fractures, offsetting the intersection and reducing its volume, an issue that should form the basis of future investigations.

6. Conclusions

The aim of this study was to quantify the hydro-mechanical properties of the intersections between fractures. This was achieved through generating intersections between two sequentially formed tensile fractures in two samples

of SB, then measuring their permeability as a function of differential pressure, and comparing this with independent fracture permeability. Our results indicate that intersecting fractures are more permeable than independent fractures by approximately one order of magnitude, and are capable of maintaining that higher permeability under conditions of increasing confining pressure, particularly above 40 MPa (equivalent to a burial pressure of 1.5 km) where macro-fracture apertures are expected to become closed. We suggest that this results from the intersection cavity being less compliant than individual macro-cracks. We propose a model of intersection permeability as a function of differential pressure by assuming that the total permeability of an intersecting system corresponds to the contributions of the two unconnected fractures plus a cavity with an elastic compressibility determined by its geometry. This simple approach allows us to examine the coupled hydro-mechanical properties of fracture intersections by determining an effective elastic compressibility for the intersection cavity normalized by the compressibility of a circular cavity, obtaining a value of $\frac{c_{\text{cavity}}}{c_{\text{circle}}} = 6.5$ for the first sample and of $\frac{c_{\text{cavity}}}{c_{\text{circle}}} = 27$ for the second one to fit their respective intersection permeability data. These are significantly lower than the compressibility expected for low aspect ratio (0.001) macro-cracks, whose compressibility is on the range of 1,000 times that of a circular cavity. Permeability measurements during cyclic loading allowed us to determine the ESL coefficient for fracture and intersection permeability, for an ESL of the form $p_e = p_c - \alpha p_p$. Results indicate that $\alpha_{\text{intersection}} = 0.81$ and $\alpha_{\text{fracture}} = 0.91$, which suggests that the channels controlling fluid flow have a higher aspect ratio (are more tubular) for the intersections relative to single fractures. Our results have significant implications for the understanding, quantification and predictability of fluid flow through fracture networks at depth, which we suggest need to be further studied and considered for up-scaling and modeling of fluid flow through fractured systems.

Data Availability Statement

Raw experimental data obtained and presented in this study is available at Stanton-Yonge et al., 2022, https://doi.org/10.5281/zenodo.7025637.

Acknowledgments
The authors would like to acknowledge Nicolas Brantut for detailed discussions that helped to guide and shape this project, and for a comprehensive review of an early version of this manuscript. Neil Hughes and Jim Davy provided technical support, and assistance from Chris Harbord and Frans Aben helped to overcome technical issues in the laboratory. The authors thank W. Ashley Griffith, Catalina Sánchez-Roa, and Michele Fondriest for helpful discussions and feedback. Detailed comments by Editor Yves Bernabe and two anonymous reviewers helped to considerably improve this manuscript. ASY acknowledges the Agencia Nacional de Investigación y Desarrollo (ANID) of Chile for funding provided through Beca Chile scholarship for PhD studies, and the three authors acknowledge financial support from the UK National Environment Research Council through Grant NE/TT007826/1.

References

Bandis, S., Lumsden, A., & Barton, N. (1983). Fundamentals of rock joint deformation. *International Journal of Rock Mechanics and Mining Sciences & Geomechanics Abstracts*, *20*, 249–268.

Benson, P. M., Meredith, P. G., Platzman, E. S., & White, R. E. (2005). Pore fabric shape anisotropy in porous sandstones and its relation to elastic wave velocity and permeability anisotropy under hydrostatic pressure. *International Journal of Rock Mechanics and Mining Sciences*, *42*(7–8), 890–899. https://doi.org/10.1016/j.ijrmms.2005.05.003

Bernabe, Y. (1986). The effective pressure law for permeability in Chelmsford granite and barre granite. *International Journal of Rock Mechanics and Mining Sciences & Geomechanics Abstracts*, *23*, 267–275.

Bernabe, Y. (1987). The effective pressure law for permeability during pore pressure and confining pressure cycling of several crystalline rocks. *Journal of Geophysical Research*, *92*(B1), 649–657. https://doi.org/10.1029/jb092ib01p00649

Brown, S. R. (1987). Fluid flow through rock joints: The effect of surface roughness. *Journal of Geophysical Research*, *92*(B2), 1337–1347. https://doi.org/10.1029/jb092ib02p01337

Brown, S. R., & Scholz, C. H. (1985). Closure of random elastic surfaces in contact. *Journal of Geophysical Research*, *90*(B7), 5531–5545. https://doi.org/10.1029/jb090ib07p05531

Brown, S. R., & Scholz, C. H. (1986). Closure of rock joints. *Journal of Geophysical Research*, *91*(B5), 4939–4948. https://doi.org/10.1029/jb091ib05p04939

Cacas, M.-C., Ledoux, E., de Marsily, G., Tillie, B., Barbreau, A., Durand, E., & Peaudecerf, P. (1990). Modeling fracture flow with a stochastic discrete fracture network: Calibration and validation: 1. The flow model. *Water Resources Research*, *26*(3), 479–489. https://doi.org/10.1029/89wr00041

Caine, J. S., Evans, J. P., & Forster, C. B. (1996). Fault zone architecture and permeability structure. *Geology*, *24*(11), 1025–1028. https://doi.org/10.1130/0091-7613(1996)024<1025:fzaaps>2.3.co;2

Cox, S. (2010). The application of failure mode diagrams for exploring the roles of fluid pressure and stress states in controlling styles of fracture-controlled permeability enhancement in faults and shear zones. *Geofluids*, *10*(1–2), 217–233. https://doi.org/10.1111/j.1468-8123.2010.00281.x

Cox, S., & Ruming, K. (2004). The St Ives mesothermal gold system, western Australia—A case of golden aftershocks? *Journal of Structural Geology*, *26*(6–7), 1109–1125. https://doi.org/10.1016/j.jsg.2003.11.025

Craw, D. (2000). Fluid flow at fault intersections in an active oblique collision zone, Southern Alps, New Zealand. *Journal of Geochemical Exploration*, *69*, 523–526. https://doi.org/10.1016/s0375-6742(00)00094-7

de Dreuzy, J.-R., Davy, P., & Bour, O. (2001). Hydraulic properties of two-dimensional random fracture networks following a power law length distribution: 2. Permeability of networks based on lognormal distribution of apertures. *Water Resources Research*, *37*(8), 2079–2095. https://doi.org/10.1029/2001wr900010

de Dreuzy, J.-R., Davy, P., & Bour, O. (2002). Hydraulic properties of two-dimensional random fracture networks following power law distributions of length and aperture. *Water Resources Research*, *38*(12), 12–21. https://doi.org/10.1029/2001WR001009

Faulkner, D., & Armitage, P. (2013). The effect of tectonic environment on permeability development around faults and in the brittle crust. *Earth and Planetary Science Letters*, *375*, 71–77. https://doi.org/10.1016/j.epsl.2013.05.006

Gangi, A. F. (1978). Variation of whole and fractured porous rock permeability with confining pressure. *International Journal of Rock Mechanics and Mining Sciences & Geomechanics Abstracts*, *15*(5), 249–257. https://doi.org/10.1016/0148-9062(78)90957-9

Gartrell, A., Zhang, Y., Lisk, M., & Dewhurst, D. (2004). Fault intersections as critical hydrocarbon leakage zones: Integrated field study and numerical modelling of an example from the Timor Sea, Australia. *Marine and Petroleum Geology*, *21*(9), 1165–1179. https://doi.org/10.1016/j.marpetgeo.2004.08.001

Gentier, S. (1986). Morphologie et comportement hydromécanique d'une fracture naturelle dans un granite sous contrainte normale: étude expérimentale et théorique. (Unpublished doctoral dissertation).

Hofmann, H., Blöcher, G., Milsch, H., Babadagli, T., & Zimmermann, G. (2016). Transmissivity of aligned and displaced tensile fractures in granitic rocks during cyclic loading. *International Journal of Rock Mechanics and Mining Sciences*, *87*, 69–84. https://doi.org/10.1016/j.ijrmms.2016.05.011

Iwai, K. (1976). *Fundamental studies of fluid flow through a single fracture*. University of California.

Jaeger, J. C., Cook, N. G., & Zimmerman, R. (2009). *Fundamentals of rock mechanics*. John Wiley & Sons.

Jones, F. O. (1975). A laboratory study of the effects of confining pressure on fracture flow and storage capacity in carbonate rocks. *Journal of Petroleum Technology*, *27*(01), 21–27. https://doi.org/10.2118/4569-pa

Kluge, C., Blöcher, G., Hofmann, H., Barnhoorn, A., Schmittbuhl, J., & Bruhn, D. (2021). The stress-memory effect of fracture stiffness during cyclic loading in low-permeability sandstone. *Journal of Geophysical Research: Solid Earth*, *126*(10), e2020JB021469. https://doi.org/10.1029/2020jb021469

Kranz, R., Frankel, A., Engelder, T., & Scholz, C. (1979). The permeability of whole and jointed barre granite. *International Journal of Rock Mechanics and Mining Sciences & Geomechanics Abstracts*, *16*(4), 225–234. https://doi.org/10.1016/0148-9062(79)91197-5

Lee, Y.-H., Carr, J., Barr, D., & Haas, C. (1990). The fractal dimension as a measure of the roughness of rock discontinuity profiles. *International Journal of Rock Mechanics and Mining Sciences & Geomechanics Abstracts*, *27*(6), 453–464. https://doi.org/10.1016/0148-9062(90)90998-h

Mandelbrot, B. B. (1982). *The fractal geometry of nature* (Vol. 1). WH Freeman.

Milsch, H., Hofmann, H., & Bloecher, G. (2016). An experimental and numerical evaluation of continuous fracture permeability measurements during effective pressure cycles. *International Journal of Rock Mechanics and Mining Sciences*, *89*, 109–115. https://doi.org/10.1016/j.ijrmms.2016.09.002

Nara, Y., Meredith, P. G., Yoneda, T., & Kaneko, K. (2011). Influence of macro-fractures and micro-fractures on permeability and elastic wave velocities in basalt at elevated pressure. *Tectonophysics*, *503*(1–2), 52–59. https://doi.org/10.1016/j.tecto.2010.09.027

Petrovitch, C. L., Nolte, D. D., & Pyrak-Nolte, L. J. (2013). Scaling of fluid flow versus fracture stiffness. *Geophysical Research Letters*, *40*(10), 2076–2080. https://doi.org/10.1002/grl.50479

Piquer, J., Yáñez, G., Rivera, O., & Cooke, D. R. (2019). Long-lived crustal damage zones associated with fault intersections in the high Andes of central Chile. *Andean Geology*, *46*(2), 223–239. https://doi.org/10.5027/andgeov46n2-3106

Pollard, D. D. (1973). Equations for stress and displacement fields around pressurized elliptical holes in elastic solids. *Journal of the International Association for Mathematical Geology*, *5*(1), 11–25. https://doi.org/10.1007/bf02114084

Pyrak-Nolte, L., & Morris, J. (2000). Single fractures under normal stress: The relation between fracture specific stiffness and fluid flow. *International Journal of Rock Mechanics and Mining Sciences*, *37*(1–2), 245–262. https://doi.org/10.1016/s1365-1609(99)00104-5

Pyrak-Nolte, L. J., & Nolte, D. D. (2016). Approaching a universal scaling relationship between fracture stiffness and fluid flow. *Nature Communications*, *7*(1), 1–6. https://doi.org/10.1038/ncomms10663

Robin, P.-Y. F. (1973). Note on effective pressure. *Journal of Geophysical Research*, *78*(14), 2434–2437. https://doi.org/10.1029/jb078i014p02434

Rowland, J., & Sibson, R. (2004). Structural controls on hydrothermal flow in a segmented rift system, Taupo volcanic zone, New Zealand. *Geofluids*, *4*(4), 259–283. https://doi.org/10.1111/j.1468-8123.2004.00091.x

Scholz, C. H., & Hickman, S. H. (1983). Hysteresis in the closure of a nominally flat crack. *Journal of Geophysical Research*, *88*(B8), 6501–6504. https://doi.org/10.1029/jb088ib08p06501

Sibson, R. H. (1996). Structural permeability of fluid-driven fault-fracture meshes. *Journal of Structural Geology*, *18*(8), 1031–1042. https://doi.org/10.1016/0191-8141(96)00032-6

Snow, D. T. (1969). Anisotropie permeability of fractured media. *Water Resources Research*, *5*(6), 1273–1289. https://doi.org/10.1029/wr005i006p01273

Stanton-Yonge, A., Mitchell Thomas, M., Meredith Philip, G. (2022). The hydro-mechanical properties of fracture intersections: Pressure dependant permeability and effective stress law (version 1) [Dataset]. *Zenodo*. https://doi.org/10.5281/zenodo.7025637

Tsang, Y. W., & Tsang, C. (1987). Channel model of flow through fractured media. *Water Resources Research*, *23*(3), 467–479. https://doi.org/10.1029/wr023i003p00467

Tsang, Y. W., & Witherspoon, P. (1981). Hydromechanical behavior of a deformable rock fracture subject to normal stress. *Journal of Geophysical Research*, *86*(B10), 9287–9298. https://doi.org/10.1029/jb086ib10p09287

Tsukrov, I., & Novak, J. (2002). Effective elastic properties of solids with defects of irregular shapes. *International Journal of Solids and Structures*, *39*(6), 1539–1555. https://doi.org/10.1016/s0020-7683(01)00285-2

Vogler, D., Amann, F., Bayer, P., & Elsworth, D. (2016). Permeability evolution in natural fractures subject to cyclic loading and gouge formation. *Rock Mechanics and Rock Engineering*, *49*(9), 3463–3479. https://doi.org/10.1007/s00603-016-1022-0

Walsh, J. (1965). The effect of cracks on the compressibility of rock. *Journal of Geophysical Research*, *70*(2), 381–389. https://doi.org/10.1029/jz070i002p00381

Walsh, J. (1981). Effect of pore pressure and confining pressure on fracture permeability. *International Journal of Rock Mechanics and Mining Sciences & Geomechanics Abstracts*, *18*(5), 429–435. https://doi.org/10.1016/0148-9062(81)90006-1

Witherspoon, P. A., Wang, J. S., Iwai, K., & Gale, J. E. (1980). Validity of cubic law for fluid flow in a deformable rock fracture. *Water Resources Research*, *16*(6), 1016–1024. https://doi.org/10.1029/wr016i006p01016

Xu, C., & Dowd, P. (2010). A new computer code for discrete fracture network modelling. *Computers & Geosciences*, *36*(3), 292–301. https://doi.org/10.1016/j.cageo.2009.05.012

Yoshioka, N. (1994). The role of plastic deformation in normal loading and unloading cycles. *Journal of Geophysical Research*, *99*(B8), 15561–15568. https://doi.org/10.1029/94jb00931

Zhao, J., & Brown, E. (1992). Hydro-thermo-mechanical properties of joints in the Carnmenellis granite. *The Quarterly Journal of Engineering Geology*, *25*(4), 279–290. https://doi.org/10.1144/gsl.qjeg.1992.025.04.03

Zimmerman, R. (1986). Compressibility of two-dimensional cavities of various shapes. *Journal of Applied Mechanics*, *53*(3), 500–504. https://doi.org/10.1115/1.3171802